PHYSICAL REVIEW A **107**, 012608 (2023)

Effect of quantum statistics on computational power of atomic quantum annealers

Yuchen Luo[1] and Xiaopeng Li[1,2,3,*]
[1]*State Key Laboratory of Surface Physics, Key Laboratory of Micro and Nano Photonic Structures (MOE), and Department of Physics, Fudan University, Shanghai 200433, China*
[2]*Institute for Nanoelectronic Devices and Quantum Computing, Fudan University, Shanghai 200433, China*
[3]*Shanghai Qi Zhi Institute, Shanghai 200232, China*

(Received 1 September 2022; revised 16 December 2022; accepted 4 January 2023; published 17 January 2023)

Quantum particle statistics fundamentally controls the way particles interact and plays an essential role in determining the properties of the system at low temperature. Here we study how the quantum statistics affects the computational power of quantum annealing. We propose an annealing Hamiltonian describing quantum particles moving on a square lattice and compare the computational performances of the atomic quantum annealers between two statistically different components: spinless fermions and hard-core bosons. In addition, we take an Ising quantum annealer driven by traditional transverse-field quantum fluctuations as a baseline. The potential of our quantum annealers to solve combinatorial optimization problems is demonstrated on random 3-regular graph partitioning. We find that the bosonic quantum annealer outperforms the fermionic case. The superior performance of the bosonic quantum annealer is attributed to larger excitation gaps and the consequent smoother adiabatic transformation of its instantaneous quantum ground states. Along our annealing schedule, the bosonic quantum annealer is less affected by the glass order and explores the Hilbert space more efficiently. Our theoretical finding could shed light on constructing atomic quantum annealers using Rydberg atoms in optical lattices.

DOI: 10.1103/PhysRevA.107.012608

I. INTRODUCTION

One of the central challenges in computer science is to design efficient algorithms to solve combinatorial optimization problems [1] that are of practical importance in a broad range of fields. Most of such computational tasks are NP-hard or NP-complete problems, which require minimizing a cost function having a large number of local minima, making it intractable for classical algorithms.

Quantum annealing [2–7] is a promising quantum computing approach that may have significant quantum speedup in solving combinatorial optimization problems. It is a heuristic algorithm that formulates the cost function into a quantum many-body Hamiltonian, typically an Ising spin Hamiltonian [8], then utilizes quantum fluctuations to escape from trapping by local minima, and explores the spin-glass-like energy landscape for the ground state that encodes the optimal solution. The theoretical foundation of quantum annealing is built on the adiabatic theorem of quantum mechanics [9,10], which ensures that the quantum system will stay close to the instantaneous ground state if the initial Hamiltonian changes into the problem Hamiltonian slowly enough, and the annealing time scales inversely proportional to a polynomial of the minimal energy gap [11–13].

Holding the expectation of quantum speedups over algorithms running on classical computers, numerous efforts have been devoted to the realization of large-scale programmable quantum devices, from superconducting qubits to trapped ions [7,14]. There have been rapid technological advances in recent years in fabricating quantum annealers having a large number of spins, which have been attracting extensive attention in industry and academia [15–17]. Nevertheless, for technical issues such as quantum decoherence and control errors, whether quantum annealing could fulfill its promise of significant quantum speedup over classical computing is still an open question. In the noisy intermediate-scale quantum era [18], developing alternative quantum annealing protocols and architectures with near-term technology is still in great demand for reaching the quantum computation advantage on combinatorial optimization problems.

With remarkable experimental progress in the past two decades, ultracold atoms in optical lattices, originally engineered as a highly controllable quantum simulator for exotic many-body physics, provide new opportunities to build a scalable quantum annealer [19,20]. In addition to refined measurement techniques, free programmability in optical lattices has been recently achieved via single-site control and cavity-mediated long-range interactions [21–29], generically necessary to carry out classical optimization on a quantum annealer. Based on the atomic platform, it is a natural choice to encode a qubit into the occupation number of a lattice site, which can be either zero or one of intrinsically repulsive spinless fermions or hard-core bosons. The atomic tunneling, in which the effect of quantum statistics is embodied, plays the role of quantum fluctuation to drive the search for the optimal occupation configurations. Quantum particle statistics, as a fundamental concept in quantum physics, is an important

---

[*] xiaopeng_li@fudan.edu.cn

factor in determining the dynamical properties of the system and can give rise to big contrasts in the nature of the ground state [30–33]. From both theoretical interests and practical considerations, it is worth pursuing the answers of the questions of which of fermionic or bosonic tunneling, serving as the driver Hamiltonian, leads to better computational performance and how the two atomic quantum annealers with different quantum statistics behave differently during annealing.

Here we propose an atomic quantum annealer under fermionic or bosonic statistics and investigate the effect of quantum statistics in this context. A commonly used model for quantum annealing is the Ising spin Hamiltonian, which is universal for classical problems [34] and has been implemented in a range of different physical platforms [15,35,36]. For this reason, we also compare the atomic quantum annealer with the Ising-model approach. To carry out a concrete analysis, we focus on the performance of the three quantum annealers to solve the random instances of 3-regular graph partitioning using a fixed amount of annealing time. By numerical simulation of the time evolution of our quantum annealers, we find that, on average, the bosonic quantum annealer reaches higher success probability than the fermionic one and the performance of the bosonic quantum annealer is comparable to the Ising-model quantum annealer. How the three quantum annealers perform is directly related to their low-energy spectra and the bottlenecks can be diagnosed by the ground-state fidelity susceptibility which measures the transformation smoothness of the instantaneous quantum ground state. Looking into their behavior during annealing, the bosonic quantum annealer is always less affected by the glass order and explores a larger portion of the many-body Hilbert space compared to the fermionic one.

The paper is organized as follows. In Sec. II we first introduce the graph partitioning problem and describe the setup of our atomic quantum annealers. In Sec. III we compare numerically the computational performances of the three quantum annealers and study several properties to illustrate their behavior difference. Finally, a discussion and conclusions are presented in Sec. IV.

II. QUANTUM ANNEALING SETUP

A. Graph partitioning

Partitioning is one of the six basic NP-complete problems proposed by Garey and Johnson in [37]. This class of problems bears close resemblance to the spin-glass problem. Studying the complexity hardness of partitioning problem and understanding the physics behind spin glasses are auxiliary to each other [38,39].

Here we focus on the well-studied problem graph partitioning [8], which is defined on an undirected graph $G = (V, E)$, with an even number $N = |V|$ of vertices connected by a set of edges $E = \{(v_i, v_j)\}$. The task is to partition the vertex set V into two subsets V_1 and V_2 with equal size $N/2$ such that the number of edges connecting V_1 and V_2 is minimized. Then the cost function can be formulated as this edge number

$$C(V_1, V_2) = \sum_{v_i \in V_1, v_j \in V_2} A_{ij}, \tag{1}$$

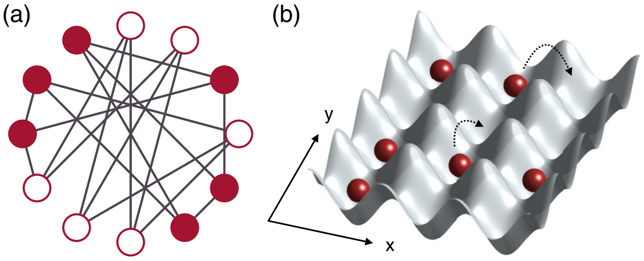

FIG. 1. (a) Illustrative example of a 12-vertex instance of 3-regular graph partitioning. Its optimal partitioning is indicated by the closed and open vertices. (b) Schematic illustration of spinless fermions or hard-core bosons in a two-dimensional optical lattice. Each lattice site represents a vertex on the graph and the site occupation denotes the corresponding vertex being in either of two subsets. The graph connectivity is embedded in the interactions between atoms and the nearest-neighbor tunneling plays the role of quantum fluctuation in the quantum adiabatic evolution.

where A_{ij} is the adjacent matrix element of the graph, equal to one when there is an edge between vertex v_i and vertex v_j and zero when there is no edge. We consider random graph instances in a specific ensemble where the degree of every vertex is set equal to 3, i.e., 3-regular graphs, and by definition each row and column of the adjacent matrix A sums to this fixed degree. Figure 1(a) shows an illustrative example of a 3-regular graph with 12 vertices and its optimal partitioning.

B. Atomic quantum annealer

Considering that spinless fermions or hard-core bosons can only occupy a lattice site by particle number zero or one, we naturally encode a qubit into a site occupation and the solutions of combinatorial optimization problems into the occupation configurations. For graph partitioning, each vertex v_i on the graph corresponds to a lattice site i and the graph connectivity is embedded in the interactions between atoms. In this way, the problem Hamiltonian in the atomic quantum annealer is of the form

$$H_{\rm P}^{\rm atomic} = \sum_{(v_i, v_j) \in E} \frac{1}{2}[1 - (1 - 2n_i)(1 - 2n_j)], \tag{2}$$

where the site occupation $n_i = \{0, 1\}$ denotes the corresponding vertex being in either of two subsets. The nonlocal graph connectivity can be realized by adopting the quantum wiring scheme [40], which has been realized by controlling Rydberg excitations in an atomic experiment [41]. As proposed in this scheme, the required long-range interaction is mediated by a ferromagnetic quantum wire coupling two distant qubits by exploiting the controllability of atomic systems. The ancilla qubits introduced as quantum wires are carefully organized such that the quantum annealing architecture can be embedded into a three-dimensional cubic lattice [40] or a two-dimensional square lattice [42] with nearest-neighbor interactions only. Since the total particle number is conserved in an atomic system, the equal-partitioning constraint is satisfied by taking the particle number to be at half filling $N_p = \sum_{i=1}^{N} n_i = N/2$. A half-filled optical lattice encoding a 12-bit problem instance is illustrated in Fig. 1(b).

The nearest-neighbor atomic tunneling on the two-dimensional lattice

$$H_{\rm T} = \sum_{\langle i,j\rangle, i<j} -(a_i^\dagger a_j + a_j^\dagger a_i) \tag{3}$$

serves as the driver Hamiltonian to provide quantum fluctuations of occupation configurations, where $\langle i, j\rangle$ labels a pair of nearest-neighbor sites and $a_i^\dagger$ (a_i) creates (annihilates) a spinless fermion or a hard-core boson at site i. The index i relates to the two-dimensional site index (m, n) by $i \equiv m + (n-1)L_x$, with $m = 1, \ldots, L_x$ ($n = 1, \ldots, L_y$) denoting the index along the x and y directions, respectively. We adopt an open boundary condition here mainly considering the experimental feasibility.

To initialize the quantum annealer with an easily implemented ground state that is unique and finitely gapped, the initial Hamiltonian is chosen to be a set of on-site potentials

$$H_{\rm V} = \sum_{i=1}^{N} V_i n_i. \tag{4}$$

We take a specific occupation configuration $|n_1 n_2 n_3 n_4 \cdots\rangle = |0101\cdots\rangle$ as its ground state by setting $V_i = -2$ for even i and $V_i = 0$ for odd i. The bias of this artificial choice is expected to be eliminated by random graph sampling.

We propose an annealing schedule that linearly interpolates from $H_{\rm V}$ to $H_{\rm P}^{\rm atomic}$ with

$$H^{\rm atomic}(s) = (1-s)H_{\rm V} + \lambda s(1-s)H_{\rm T} + sH_{\rm P}^{\rm atomic}. \tag{5}$$

Here the Hamiltonian $H_{\rm T}$ is introduced to generate quantum fluctuations. This is necessary in our scheme because the initial and final Hamiltonians commute, i.e., $[H_{\rm V}, H_{\rm P}^{\rm atomic}] = 0$. The parameter $s(t) = t/\mathcal{T} \in [0, 1]$ determines the annealing path with the total annealing time $\mathcal{T}$, and the parameter λ, set to be $\lambda = 3$, controls the driving strength. Our annealing schedule follows the same time-dependent form of reverse annealing [43–47], which is proposed to enhance performance via choosing an appropriate initial state. In contrast, we take a specific configuration as an initial state just out of consideration for experimental implementation on an atomic platform and the initial configuration can be any convenient choice.

The quantum statistics of an atomic quantum annealer is practically determined by whether the particles loaded into optical lattices are fermions (e.g., ^{6}Li [29,48,49], ^{40}K [50–52], and ^{173}Yb [53]) or bosons (e.g., ^{87}Rb [54,55] and ^{133}Cs [56,57]). We consider two atomic quantum annealers that are assembled with spinless fermions and hard-core bosons, respectively, in order to investigate the effect of quantum statistics on the annealing performance. Although their annealing processes are described by a Hamiltonian of the same form (5), the two annealers are fundamentally different, for the underlying quantum particles obey different statistics. This difference can be readily seen via the Jordan-Wigner transformation [58] of the atomic tunneling term. The bosonic tunneling is equivalent to the XXZ model defined on the same two-dimensional (2D) lattice

$$H_{\rm T,JW}^{\rm Bose} = \sum_{\langle i,j\rangle, i<j} -\frac{1}{2}\left(\sigma_i^x\sigma_j^x + \sigma_i^y\sigma_j^y\right). \tag{6}$$

The XXZ-model-based quantum annealing has been suggested for performing constrained optimization [59]. Fermionic anticommutation rules, as the consequence of Fermi-Dirac statistics, give rise to the appearance of nonlocal Jordan-Wigner strings in the transformation. The resulting 2D Ising model has nonlocal interactions between spins

$$H_{\rm T,JW}^{\rm Fermi} = \sum_{\langle i,j\rangle, i<j} -\frac{i}{2}\left(\prod_{k=i}^{j-1}\sigma_k^z\right)\left(\sigma_i^y\sigma_j^x + \sigma_i^x\sigma_j^y\right), \tag{7}$$

which explicitly shows highly nontrivial sign structures for the Hamiltonian matrix in the computational basis. Although both Ising-form Hamiltonians (6) and (7) conserve the total magnetization $S_z = \sum_{i=1}^N \sigma_i^z$, i.e., $[H_{\rm T,JW}, S_z] = 0$, their quantum dynamics are drastically different.

It is not *a priori* clear whether the nonlocal Fermi sign structure would be helpful or harmful to the quantum annealing [60–64]. On the one hand, it generates nonlocal couplings, which would tend to make the many-body system more ergodic and potentially weaken the spin-glass problem [65]; on the other hand, it involves nonstoquastic Hamiltonians at intermediate times whose ground states are in general difficult to reach [66–68].

C. Ising quantum annealer

Encoded as an Ising model, the problem Hamiltonian for graph partitioning consists of two parts

$$H_{\rm P}^{\rm Ising} = \sum_{(v_i,v_j)\in E} \frac{1}{2}\left(1 - \sigma_i^z\sigma_j^z\right) + \alpha\left(\sum_{i=1}^{N}\sigma_i^z\right)^2, \tag{8}$$

where the first term carries the energy cost of edges connecting vertices from different subsets and the second provides an energy penalty representing the size imbalance of the two subsets. In order to ensure the balancing constraint in the equal-partition problem, the factor α for graph partitioning must satisfy the condition $\alpha \geqslant \frac{1}{8}\min(2\Delta, N)$, with Δ the maximal degree of graph [8]. We choose a fairly small value for $\alpha = 1$ that satisfies this condition, as a too large penalty would suppress quantum fluctuations in the adiabatic quantum evolution and make the quantum annealing inefficient.

Since we focus on analyzing the effect of quantum statistics on the quantum annealing in this study, we take a Hamiltonian schedule for the Ising-model-based quantum annealing,

$$H^{\rm Ising}(s) = (1-s)H_{\rm Z} + \lambda s(1-s)H_{\rm X} + sH_{\rm P}^{\rm Ising}. \tag{9}$$

This Hamiltonian schedule is chosen to be similar to the atomic quantum annealer in Eq. (5) for a fair comparison. The Hamiltonian schedule starts from the longitudinal-field Hamiltonian

$$H_{\rm Z} = \sum_{i=1}^{N} h_i\sigma_i^z, \tag{10}$$

where on-site fields have equal amplitude but alternating signs, $h_i = -1$ for even i and $h_i = 1$ for odd i, in correspondence with the initial potential (4) of the atomic quantum annealer. At intermediate time with $0 < s < 1$, we have introduced the transverse-field Hamiltonian $H_{\mathrm{X}} = -\sum_{i=1}^{N} \sigma_i^x$ to drive quantum fluctuations. This Ising quantum annealer offers a performance reference point to benchmark the fermionic and bosonic atomic quantum annealers.

III. NUMERICAL RESULTS

In what follows, we present the numerical results on close-system quantum annealing and compare the computation performances of the fermionic, bosonic, and Ising quantum annealers. The computation performance is obtained by simulating the quantum time evolution based on the Schrödinger equation. Then we investigate their relevant low-energy properties by exact diagonalization, aiming at characterizing the performance difference among the three quantum annealers.

A. Success probability

Aiming at comparing the computation performances of different theoretical models with different quantum statistics, we characterize the computation performance of quantum annealers by the success probability. This quantity is defined as the total probability of finding the correct solution in the projective measurement of the final quantum state $|\psi_{\mathrm{f}}\rangle$,

$$P_{\mathrm{s}}(\mathcal{T}) = \sum_{i=1}^{D} \left|\left\langle \psi_{\mathrm{s}}^{i} \middle| \psi_{\mathrm{f}} \right\rangle\right|^2, \tag{11}$$

with $|\psi_{\mathrm{s}}^{i}\rangle$ the ground states of the final Hamiltonian, $i = 1, 2, \ldots, D$ labeling the ground-state degeneracy. When it comes to investigating the performance of the actual realization on quantum computing hardware, time to solution [69] is a preferred metric, especially for comparing different quantum computing platforms having different computation timescales. Nonetheless, since we aim at studying the computation performance of quantum annealers caused by different quantum statistics, we use the success probability (11) in comparing the bosonic, fermionic, and Ising quantum annealers.

We study three problem sizes with the 2D lattice geometries $N = 4 \times 3$, 4×4, and 4×5 and sample 1000 random instances of the 3-regular graph for each system size. Each graph instance is generated by randomly adding an edge between a pair of vertices with the constraint that each vertex is connected with exactly three other different vertices and then saved in the form of an adjacent matrix. We exclude the repeated graphs by checking whether there are two identical adjacent matrices. With that, there still remain a small number of equivalent graphs related by permutation of vertices. We note that the initial state of the quantum adiabatic evolution does not respect the permutation symmetry, so the quantum annealing performances on equivalent graphs are actually not identical. The total annealing time is set equal to $\mathcal{T} = 50$, and for each instance we calculate the success probabilities of our fermionic, bosonic, and Ising quantum annealers. The performance comparison among the three quantum annealers is presented in Fig. 2. As shown in Fig. 2(a), the fermionic quantum annealer has the worst performance for all problem sizes compared to bosonic and Ising quantum annealers. The performances of the bosonic and Ising quantum annealers are more or less comparable. Focusing on the problem size $N = 4 \times 4$, we then look into the success probability for each instance and compare the success probability distributions of the three quantum annealers. The pairwise comparisons of the individual success probabilities are shown in Figs. 2(b)–2(d), and the instances with different solution degeneracy are represented by the symbols of different colors and shapes. For almost all instances (97.3%), the success probabilities of the bosonic quantum annealer are higher than those of the fermionic annealer. Comparing the two atomic quantum annealers with the Ising quantum annealer, the fermionic annealer produces higher success probabilities than the Ising annealer only for very rare instances with a small percentage of 0.095%, whereas the rate of the bosonic quantum annealer outperforming the Ising annealer is significant, reaching 36.4%. There are a number of problem instances for which the bosonic quantum annealer far outperforms the Ising annealer.

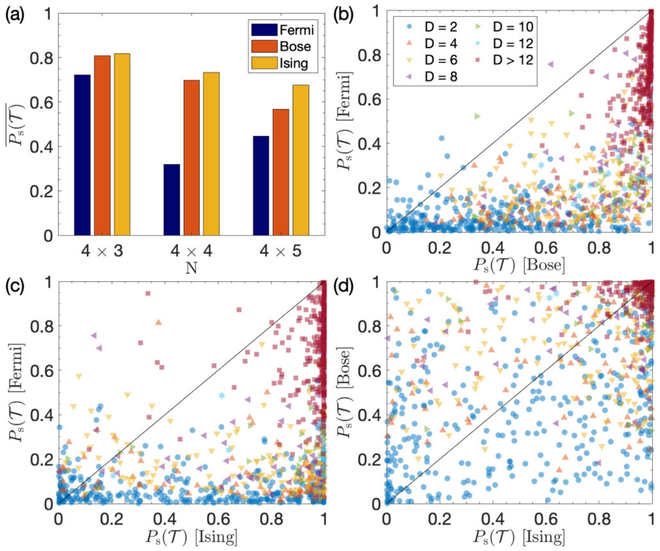

FIG. 2. Success probabilities of our fermionic, bosonic, and Ising quantum annealers with the total annealing time $\mathcal{T} = 50$. (a) Instance-averaged success probabilities of the three quantum annealers for the problem sizes $N = 4 \times 3$, 4×4, and 4×5. The individual success probabilities for the problem size $N = 4 \times 4$ are compared between (b) the fermionic and bosonic quantum annealers, (c) the fermionic and Ising quantum annealers, and (d) the bosonic and Ising quantum annealers. Each symbol represents one instance and its color and shape denote the solution degeneracy D of this instance.

For our three quantum annealers, the individual success probabilities exhibit consistent correlations with the solution degeneracy D. As a result of the bit-flip symmetry of graph partitioning $\sigma_i^z \to -\sigma_i^z$, the solution degeneracy D only takes even numbers and the two final ground states up to a bit flip produce two equivalent partition solutions. The solution degeneracy D of our generated instances for the problem size $N = 4 \times 4$ has a broad distribution from $D = 2$ up to $D = 96$. The distribution of D is shown in Fig. 3(a). The problem instances with $D = 2$, i.e., having one unique partition solution, count as $\frac{1}{3}$ of all instances. We then divide all problem instances into different classes according to the degeneracy D

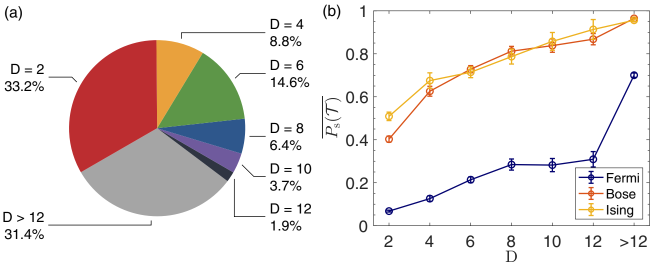

FIG. 3. (a) Solution degeneracy distribution of our 1000 problem instances for the system size $N = 4 \times 4$. (b) Success probabilities of our fermionic, bosonic, and Ising quantum annealers for the problem size $N = 4 \times 4$, which are averaged over the instances with the same solution degeneracy D and presented as functions of D.

and average over the quantum annealing success probability within each class. The results are shown in Fig. 3(b). We find consistent correlations between the success probability and the solution degeneracy for the average success probabilities of all three quantum annealers, in all of which the success probability grows monotonically with D. This implies that solving partitioning problems by quantum annealing becomes less difficult as the number of its solutions gets larger. For problem instances with a solution degeneracy D, diabatic transitions during the quantum dynamical evolution among the lowest D states will not compromise the final success probability because all of them will evolve into the ground-state manifold of the problem Hamiltonian at the end of the annealing [70]. The fermionic quantum annealer has much lower average success probabilities than the bosonic and Ising ones for all classes of different solution degeneracies. The overall performance of the bosonic quantum annealer is comparable to the Ising case.

The above comparison of success probabilities indicates that the bosonic tunneling, which drives the quantum fluctuations at intermediate time, possesses stronger computational power than the fermionic tunneling. The computation performance of the bosonic quantum annealer is comparable to the Ising model. One common feature between bosonic and Ising quantum annealers is that their Hamiltonians in the computational basis are both stoquastic [71]. This is in sharp contrast to the fermionic quantum annealer, where the Hamiltonian is nonstoquastic.

B. Relevant gap and low-energy property

A fundamental limitation on the successful probability of quantum annealing is posed by the quantum adiabatic theorem [9,10]. Despite various attempts to circumvent the adiabatic requirement by Hamiltonian path design [72–77], finding optimized Hamiltonian protocols for generic computation problems is in general difficult. The required annealing time is largely determined by the inverse of the minimum gap between the instantaneous ground state and first excited state. This energy gap thus characterizes the computation hardness of quantum annealing. In our situation where the ground state of the problem Hamiltonian is degenerate, it is reasonable to define a relevant gap between the instantaneous ground state and the first excited state outside the degenerate ground-state subspace,

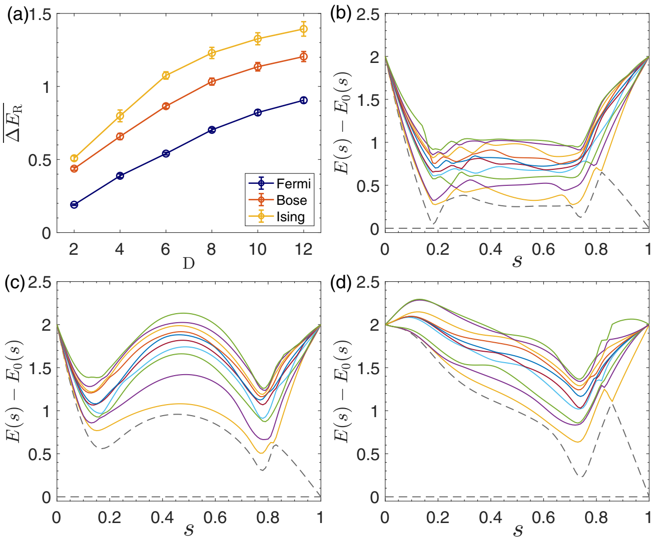

FIG. 4. (a) Relevant gaps of the interpolating Hamiltonians followed by the fermionic, bosonic, and Ising quantum annealers to solve the problem with size $N = 4 \times 4$, which are averaged over the instances with the same solution degeneracy D and presented as functions of D. Also shown are the 12 lowest energy levels of the interpolating Hamiltonians in solving a specific problem instance by the (b) fermionic, (c) bosonic, and (d) Ising quantum annealers. This instance, as a typical example, is randomly chosen. The two lowest gray dashed lines represent the energy levels converging to the two-degenerate ground states of the problem Hamiltonian and the other colored solid lines correspond to excited states.

$$\Delta E_{\mathrm{R}} = \min_{s\in[0,1]}[E_D(s) - E_0(s)], \tag{12}$$

which sets an upper bound for the minimum gap between the ground state and the first excited state of the instantaneous Hamiltonian during the whole annealing process.

Along our annealing schedule to solve the problem with size $N = 4 \times 4$, the relevant gaps are numerically determined for each instance and averaged over the instances with the same solution degeneracy D. The results for our three quantum annealers are presented in Fig. 4(a) as functions of D. We observe a systematic increase in the averaged relevant gap with the solution degeneracy, which is consistent with the behavior of success probability as shown in Fig. 3(b). A larger solution degeneracy makes it more difficult for the quantum annealer to excite out of the subspace of the lowest D states and thus help the system stay in this low-energy subspace, morphing into the ground-state manifold at the end of the quantum annealing. The fermionic quantum annealer is found to have the smallest relevant gaps for all the solution degeneracies, which we expect to be the main reason for its computation performance being the worst compared to the bosonic and Ising models. Consequently, the required evolution time for the fermionic quantum annealer to reach a certain success probability threshold is expected to be significantly larger than for the other two cases.

We further concentrate on the problem instances with $D = 2$, the largest proportion and the hardest to solve, and look into their low-energy properties relating to the performance difference. Since the performance of quantum annealing can be directly reflected by the low-energy spectrum, we randomly choose a problem instance and show the typical structure of the low-energy levels of the interpolating Hamiltonians to solve this instance by the three quantum annealers in Figs. 4(b)–4(d). For our two atomic quantum annealers, there are two minimum gaps located at the two stages where quantum fluctuations are turning on and off. The minimum gaps of the fermionic quantum annealer are much smaller than the bosonic annealer. In addition, the low-energy spectrum of the fermionic quantum annealer, compared to that of the bosonic one, has a denser structure and involves more level crossings during the annealing process. The Ising quantum annealer has a low-energy spectrum very different from the atomic ones. It develops only one minimum gap at the late stage where quantum fluctuations are turning off. The features of the low-energy spectra are expected to be generic for the three quantum annealers in solving different problem instances. This is demonstrated by investigating a number of independent problem instances (see Appendix A).

Gap closing during the annealing process is generally induced by a quantum phase transition [78–81]. Among various probes of the quantum phase transition, the ground-state fidelity susceptibility per site is a universal indicator, regardless of the transition mechanism, to locate the quantum critical point and the attendant minimum gap [82]. This quantity is defined as the second derivative of the fidelity $\mathcal{F}(s, s+\delta s) = |\langle\psi_{\rm g}(s)|\psi_{\rm g}(s+\delta s)\rangle|$ to measure the degree of criticality by the rapidity of the ground-state variation as a function of the system parameters:

$$\mathcal{S}(s) = \lim_{\delta s\to 0}\frac{-2\ln\mathcal{F}(s+\delta s)}{N(\delta s)^2}. \tag{13}$$

A peak in this fidelity susceptibility signals approaching a certain quantum critical point where the ground-state wave function changes dramatically. It is more difficult to maintain quantum adiabaticity at high $\mathcal{S}(s)$.

The average ground-state fidelity susceptibility per site along the annealing process to solve the instances with $N = 4\times 4$ and $D = 2$ by our three quantum annealers is shown in Fig. 5. For the atomic quantum annealers, two obvious peaks in the fidelity susceptibility occur, corresponding to the two minimum gaps at the two stages with quantum fluctuations turning on and off, respectively. The peaks for bosonic quantum annealer, especially the first one, are less prominent than the fermionic one, which indicates that the ground state of the bosonic quantum annealer transforms more smoothly along the annealing process. As expected, the fidelity susceptibility of the Ising quantum annealer increases significantly at the appearance of its minimum gap and the peak value is comparable to that of the bosonic annealer at the same location.

Although a general framework describing the quantum annealing efficiency is absent, it is widely believed that quantum annealing might be bottlenecked by the glass phase [83]. The glass phase appears below some critical value of quantum fluctuations and is characterized by an energy spectrum near the ground state. In this phase, small changes in Hamiltonian parameters may lead to a chaotic reordering of associated energy levels, which causes level crossings with exponentially small energy gaps. In order to examine the glass physics in the quantum annealers, we calculate the Edwards-Anderson order parameters of the glass phase [84]. For the atomic quantum annealers, we measure the fluctuations of occupation numbers on each lattice site,

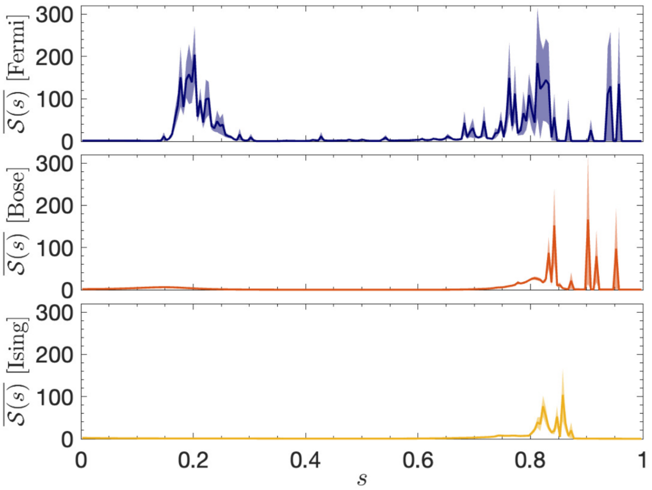

FIG. 5. Ground-state fidelity susceptibilities per site along the annealing process of the fermionic, bosonic, and Ising quantum annealers, which are averaged over the instances with $N = 4\times 4$ and $D = 2$.

$$q_n = \frac{1}{N}\sum_{i=1}^{N}\langle 2n_i - 1\rangle^2. \tag{14}$$

For the Ising quantum annealer, we measure the fluctuations of spin orientation

$$q_z = \frac{1}{N}\sum_{i=1}^{N}\langle\sigma_i^z\rangle^2. \tag{15}$$

These two expressions are both normalized to the range of [0,1].

The glass order strength along the annealing process of the three quantum annealers is shown in Fig. 6, which is averaged over different problem instances with $N = 4\times 4$ and $D = 2$. We calculate the ground-state glass order as well as the low-energy glass order that is averaged over the 12 lowest eigenstates of the interpolating Hamiltonian. The two quantities involving the low-energy states are largely related to the performance of quantum annealers. Along the whole annealing process, from an initial product state to the final ground state, the bosonic quantum annealer is consistently less affected by the glass order compared to the fermionic one. This is consistent with our observation on the low-energy spectra in Figs. 4(b) and 4(c), where the bosonic quantum annealer develops fewer anticrossings. Although the comparable computation performance is with the bosonic quantum annealer, the Ising quantum annealer always stays in stronger glass order, indicating its instantaneous states are very different from the bosonic ones.

C. Annealing dynamical behavior

We further investigate the difference of the three quantum annealers in terms of the dynamical behavior. The problem instances with $N = 4\times 4$ and $D = 2$ are still taken for

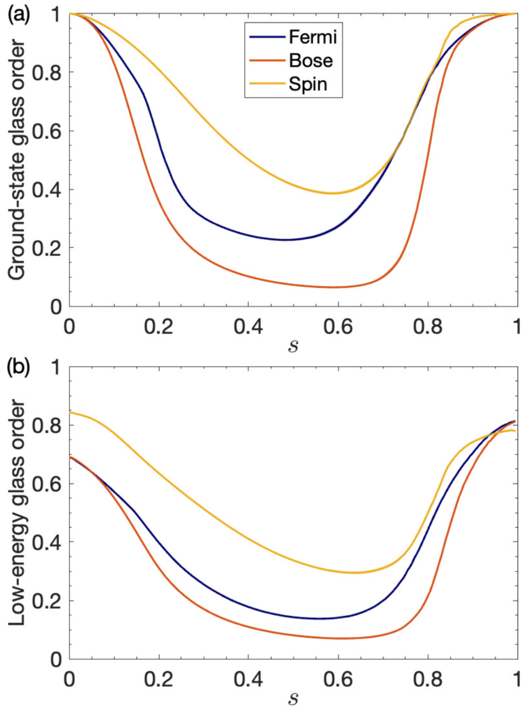

FIG. 6. (a) Ground-state glass order and (b) average glass order of the 12 lowest eigenstates along the annealing process of the fermionic, bosonic, and Ising quantum annealers. Both are averaged over the instances with $N = 4 \times 4$ and $D = 2$.

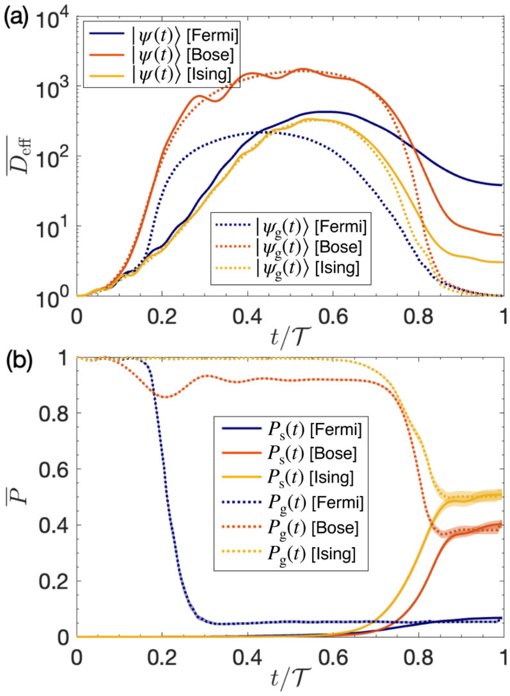

FIG. 7. (a) Effective dimensions of the time-evolving state $|\psi(t)\rangle$ (solid lines), with the ones of the instantaneous ground state $|\psi_g(t)\rangle$ (dotted lines) as an adiabatic reference, and (b) instantaneous values of the success probability (solid lines) and the ground-state probability (dotted lines) along the annealing process of the fermionic, bosonic, and Ising quantum annealers. The above results are averaged over the instances with $N = 4 \times 4$ and $D = 2$.

illustration. We calculate the effective dimension of the dynamical state, which characterizes how efficiently the intermediate dynamical state explores the entire Hilbert space. It is defined as

$$D_{\mathrm{eff}}(|\psi\rangle) = \left(\sum_{i=1}^{\mathcal{D}} |c_i|^4 \right)^{-1}, \tag{16}$$

where the c_i are the amplitudes of the state $|\psi\rangle$ on each computational basis and $\mathcal{D}$ is the dimension of the Hilbert space. This quantity has been widely used in the study of delocalization or thermalization [85–87].

We consider the effective dimensions of the time-evolving state $|\psi(t)\rangle$ along the annealing process for each quantum annealer, with the ones of the instantaneous ground state $|\psi_g(t)\rangle$ as an adiabatic reference. The results are shown in Fig. 7(a). All of the three quantum annealers drive their initial states to a large fraction of the Hilbert space as quantum fluctuation turns on. The quantum dynamical state gradually converges to the solution configurations with the ramp-off of the quantum fluctuation. The bosonic quantum annealer expands its dynamical state to the large Hilbert space with a faster rate than the fermionic annealer. The resultant peak value of the effective dimension at the intermediate time is also significantly larger for the bosonic quantum annealer than for the fermionic case. Although the value of effective dimensions of the Ising quantum annealer is significantly smaller than that of the bosonic annealer, their qualitative behaviors are similar. For both of them, with the ramp-up of quantum fluctuations, the dynamical quantum state follows closely with the instantaneous ground state and the increase of the effective dimensions in the dynamical state agrees with the instantaneous ground state. This is in sharp contrast to the fermionic quantum annealer where the effective dimension of the dynamical state deviates significantly from the instantaneous ground state.

Furthermore, we look into the instantaneous values of the success probability and the ground-state probability along the annealing process of our three quantum annealers. The success probability $P_s(t)$ follows the definition of Eq. (11) and the instantaneous ground state probability $P_g(t)$ is defined as the probability of the time-evolving state $|\psi(t)\rangle$ populating on the instantaneous ground state $|\psi_g(t)\rangle$,

$$P_g(t) = |\langle\psi_g(t)|\psi(t)\rangle|^2. \tag{17}$$

As shown in Fig. 7(b), the success probabilities $P_s(t)$ of all three quantum annealers stay almost vanishing for about half of the annealing process and then increase at different rates to their final success probabilities $P_s(\mathcal{T})$ as the annealing Hamiltonian approaches the problem Hamiltonian. Regarding the ground-state probability $P_g(t)$, the three quantum annealers exhibit distinct behaviors within our annealing time. The value of the bosonic quantum annealer goes through two obvious drops: one relatively smooth drop near the beginning and the other a steeper drop near the final. The fermionic quantum annealer develops an abrupt drop at the early stage and its ground-state probability remains small until the end. As for the Ising quantum annealer, its ground-state probability $P_g(t)$ does not drop until a late time when quantum fluctuations are turning off. The dynamical behaviors of the ground-state probability $P_g(t)$ of the three quantum annealers are consistent with our observations on their minimum gaps in Figs. 4(b)–4(d) and the deviations of their effective dimensions in Fig. 7(a).

The localization property shown by the effective dimension [88,89] in Fig. 7(a), which is expected to compromise the performance of adiabatic quantum computing at large scale [68,90], does not exhibit an evident correlation with the success probability shown in Fig. 7(b). This suggests localization may not be the key factor that determines the performance of moderate-size adiabatic quantum computing.

IV. DISCUSSION AND CONCLUSION

In this work we have carried out a systematic analysis of the effect of quantum statistics on the computational power of atomic quantum annealers. We proposed an annealing schedule for our atomic quantum annealers, and the effect of quantum statistics is embodied in the driver Hamiltonian, i.e., the fermionic or bosonic tunneling. In addition, an Ising quantum annealer was considered to provide a performance reference. The performance comparison among the three quantum annealers was demonstrated by solving random problem instances of 3-regular graph partitioning in a fixed annealing time. For all the problem sizes considered, the numerical results of their final success probabilities showed that the bosonic quantum annealer outperforms the fermionic one, reaching a performance comparable to the Ising quantum annealer.

To shed light on the difference among the three quantum annealers, we studied the problem instances with $N = 4 \times 4$ as an illustration and further concentrated on the subset with $D = 2$ for more details. The computational performance of the three quantum annealers was largely determined by their minimum gaps, which were reflected by their low-energy spectra. For two atomic quantum annealers, two minimum gaps emerged respectively when the quantum fluctuations were turned on and off. The first minimum gap of the fermionic quantum annealer was much smaller than that of the bosonic annealer, which was the major bottleneck of its computational performance. The Ising quantum annealer had only one minimum gap at the late stage when quantum fluctuations were turning off. The emergence of their minimum gaps was consistent with the peaks in their ground-state fidelity susceptibility, which measures the smoothness of the state transformation during the annealing. Along our annealing schedule, the bosonic quantum annealer suffered from weaker glass order and explored the Hilbert space more extensively than the fermionic one.

From the consideration of experimental realization, the atomic quantum annealer is particularly suitable for optimization problems with the constraint of the form $\sum_{i=1}^{N} \sigma_i^z = c$, which is automatically satisfied under particle conservation. For the traditional Ising quantum annealer, it is a standard method to impose constraints by adding penalty terms [8]. The penalty terms generally require all-to-all connectivity, which presents an enormous challenge to the near-term quantum device. The atomic quantum annealer is free of all complications resulting from penalty terms and reduces dramatically the resources to encode a problem.

ACKNOWLEDGMENTS

This work was supported by National Program on Key Basic Research Project of China (Grant No. 2021YFA1400900), National Natural Science Foundation of

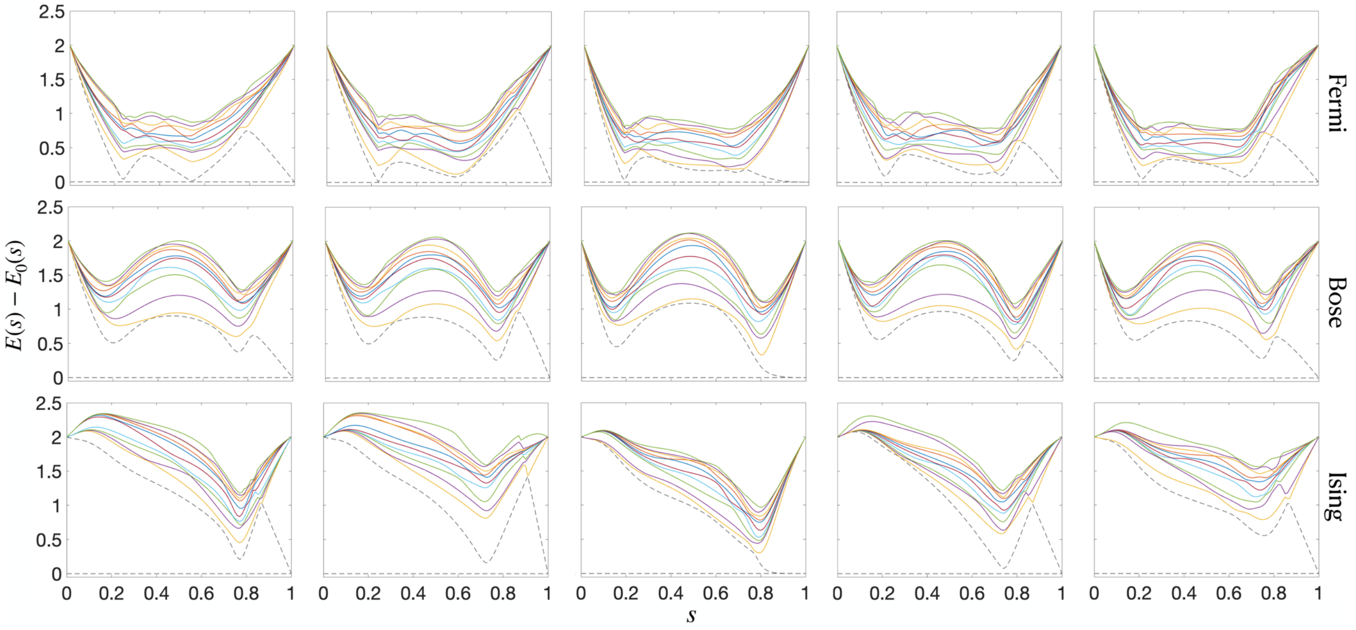

FIG. 8. The 12 lowest energy levels of the interpolating Hamiltonians in solving different problem instances by the fermionic (top row), bosonic (middle row), and Ising (bottom row) quantum annealers. The instance is taken to be the same in each column, and these five instances are randomly chosen from the instance class with $N = 4 \times 4$ and $D = 2$. The two lowest gray dashed lines represent the energy levels converging to the two-degenerate ground states of the problem Hamiltonian and the other colored solid lines correspond to excited states.

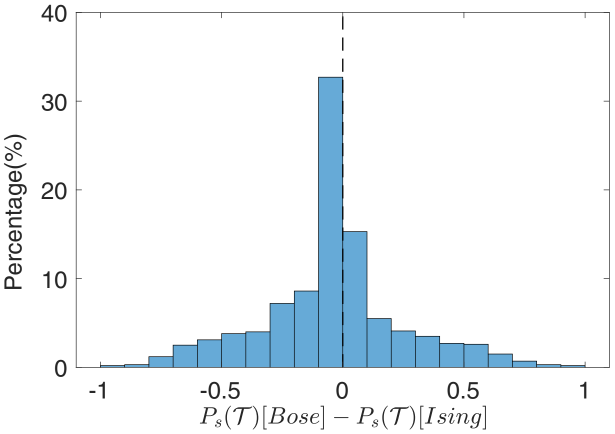

FIG. 9. Distribution of the success probability difference between the bosonic and Ising quantum annealers in solving 1000 random instances with $N = 4 \times 4$ and $\mathcal{T} = 50$.

China (Grants No. 11774067 and No. 11934002), Shanghai Municipal Science and Technology Major Project (Grant No. 2019SHZDZX01), and Shanghai Rising Star Program (Grant No. 21QA1400500).

APPENDIX A: GENERIC FEATURES OF LOW-ENERGY SPECTRA FOR OUR THREE QUANTUM ANNEALERS

Here we illustrate that the features of the low-energy spectra shown in Figs. 4(b)–4(d) are generic for the quantum annealers in solving different problem instances. We have checked this generality for many problem instances and randomly chosen five of them as an illustration. In Fig. 8 we provide the low-energy spectra of the interpolating Hamiltonians of the three quantum annealers. For all three quantum annealers, including Ising, bosonic, and fermionic, we confirm that the low-energy spectra indeed have a similar behavior as described in Sec. III B.

APPENDIX B: COMPLEMENTARY COMPUTATIONAL POWER OF BOSONIC AND ISING QUANTUM ANNEALERS

We provide in Fig. 9 the histogram of the success probability difference between the bosonic and Ising quantum annealers in solving 1000 random instances with $N = 4 \times 4$ and $\mathcal{T} = 50$. As shown in Fig. 9, the success probability differences between the two approaches have a roughly symmetric distribution and are concentrated in the range $-0.1 \leqslant P_s(\mathcal{T})[\text{Bose}] - P_s(\mathcal{T})[\text{Ising}] < 0.1$. The problem instances falling in this range count as 48.0%. There are indeed some relatively rare problem instances for which one significantly outperforms the other. These problem instances are very much symmetrically distributed. This implies bosonic and Ising quantum annealers are complementary in solving difficult optimization problems. Whether there are underlying principles to select one from these two annealers based on the problem features is worth studying further, for example, with machine-learning-based automated algorithm selection. This is left for future investigation.

---

[1] C. H. Papadimitriou and K. Steiglitz, *Combinatorial Optimization: Algorithms and Complexity* (Dover, New York, 2013).
[2] T. Kadowaki and H. Nishimori, Quantum annealing in the transverse Ising model, Phys. Rev. E **58**, 5355 (1998).
[3] E. Farhi, J. Goldstone, S. Gutmann, J. Lapan, A. Lundgren, and D. Preda, A quantum adiabatic evolution algorithm applied to random instances of an NP-complete problem, Science **292**, 472 (2001).
[4] G. E. Santoro, R. Martoňák, E. Tosatti, and R. Car, Theory of quantum annealing of an Ising spin glass, Science **295**, 2427 (2002).
[5] A. Das and B. K. Chakrabarti, *Colloquium*: Quantum annealing and analog quantum computation, Rev. Mod. Phys. **80**, 1061 (2008).
[6] T. Albash and D. A. Lidar, Adiabatic quantum computation, Rev. Mod. Phys. **90**, 015002 (2018).
[7] P. Hauke, H. G. Katzgraber, W. Lechner, H. Nishimori, and W. D. Oliver, Perspectives of quantum annealing: Methods and implementations, Rep. Prog. Phys. **83**, 054401 (2020).
[8] A. Lucas, Ising formulations of many NP problems, Front. Phys. **2**, 5 (2014).
[9] T. Kato, On the adiabatic theorem of quantum mechanics, J. Phys. Soc. Jpn. **5**, 435 (1950).
[10] A. Messiah, *Quantum Mechanics* (North-Holland, Amsterdam, 1962).
[11] S. Jansen, M.-B. Ruskai, and R. Seiler, Bounds for the adiabatic approximation with applications to quantum computation, J. Math. Phys. **48**, 102111 (2007).
[12] S. Morita and H. Nishimori, Mathematical foundation of quantum annealing, J. Math. Phys. **49**, 125210 (2008).
[13] D. A. Lidar, A. T. Rezakhani, and A. Hamma, Adiabatic approximation with exponential accuracy for many-body systems and quantum computation, J. Math. Phys. **50**, 102106 (2009).
[14] E. Altman, K. R. Brown, G. Carleo, L. D. Carr, E. Demler, C. Chin, B. DeMarco, S. E. Economou, M. A. Eriksson, K.-M. C. Fu, M. Greiner, K. R. Hazzard, R. G. Hulet, A. J. Kollár, B. L. Lev, M. D. Lukin, R. Ma, X. Mi, S. Misra, C. Monroe *et al.*, Quantum simulators: Architectures and opportunities, PRX Quantum **2**, 017003 (2021).
[15] M. W. Johnson, M. H. S. Amin, S. Gildert, T. Lanting, F. Hamze, N. Dickson, R. Harris, A. J. Berkley, J. Johansson, P. Bunyk, E. M. Chapple, C. Enderud, J. P. Hilton, K. Karimi, E. Ladizinsky, N. Ladizinsky, T. Oh, I. Perminov, C. Rich, M. C. Thom *et al.*, Quantum annealing with manufactured spins, Nature (London) **473**, 194 (2011).
[16] S. Boixo, T. Albash, F. M. Spedalieri, N. Chancellor, and D. A. Lidar, Experimental signature of programmable quantum annealing, Nat. Commun. **4**, 2067 (2013).
[17] S. Boixo, T. F. Rønnow, S. V. Isakov, Z. Wang, D. Wecker, D. A. Lidar, J. M. Martinis, and M. Troyer, Evidence for quantum

annealing with more than one hundred qubits, Nat. Phys. **10**, 218 (2014).

[18] J. Preskill, Quantum computing in the NISQ era and beyond, Quantum **2**, 79 (2018).

[19] C. Gross and I. Bloch, Quantum simulations with ultracold atoms in optical lattices, Science **357**, 995 (2017).

[20] F. Schäfer, T. Fukuhara, S. Sugawa, Y. Takasu, and Y. Takahashi, Tools for quantum simulation with ultracold atoms in optical lattices, Nat. Rev. Phys. **2**, 411 (2020).

[21] G. Gauthier, I. Lenton, N. M. Parry, M. Baker, M. J. Davis, H. Rubinsztein-Dunlop, and T. W. Neely, Direct imaging of a digital-micromirror device for configurable microscopic optical potentials, Optica **3**, 1136 (2016).

[22] M. McDonald, J. Trisnadi, K.-X. Yao, and C. Chin, Superresolution Microscopy of Cold Atoms in an Optical Lattice, Phys. Rev. X **9**, 021001 (2019).

[23] S. Subhankar, Y. Wang, T.-C. Tsui, S. L. Rolston, and J. V. Porto, Nanoscale Atomic Density Microscopy, Phys. Rev. X **9**, 021002 (2019).

[24] A. Mazurenko, C. S. Chiu, G. Ji, M. F. Parsons, M. Kanász-Nagy, R. Schmidt, F. Grusdt, E. Demler, D. Greif, and M. Greiner, A cold-atom Fermi-Hubbard antiferromagnet, Nature (London) **545**, 462 (2017).

[25] W. Yi, A. J. Daley, G. Pupillo, and P. Zoller, State-dependent, addressable subwavelength lattices with cold atoms, New J. Phys. **10**, 073015 (2008).

[26] X. Qiu, J. Zou, X. Qi, and X. Li, Precise programmable quantum simulations with optical lattices, npj Quantum Inf. **6**, 87 (2020).

[27] V. Torggler, S. Krämer, and H. Ritsch, Quantum annealing with ultracold atoms in a multimode optical resonator, Phys. Rev. A **95**, 032310 (2017).

[28] V. Torggler, P. Aumann, H. Ritsch, and W. Lechner, A quantum N-queens solver, Quantum **3**, 149 (2019).

[29] E. Guardado-Sanchez, B. M. Spar, P. Schauss, R. Belyansky, J. T. Young, P. Bienias, A. V. Gorshkov, T. Iadecola, and W. S. Bakr, Quench Dynamics of a Fermi Gas with Strong Nonlocal Interactions, Phys. Rev. X **11**, 021036 (2021).

[30] A. B. Kuklov and B. V. Svistunov, Counterflow Superfluidity of Two-Species Ultracold Atoms in a Commensurate Optical Lattice, Phys. Rev. Lett. **90**, 100401 (2003).

[31] L. F. Santos and M. Rigol, Onset of quantum chaos in one-dimensional bosonic and fermionic systems and its relation to thermalization, Phys. Rev. E **81**, 036206 (2010).

[32] E. Khatami and M. Rigol, Effect of particle statistics in strongly correlated two-dimensional Hubbard models, Phys. Rev. A **86**, 023633 (2012).

[33] W. Nie, H. Katsura, and M. Oshikawa, Particle statistics, frustration, and ground-state energy, Phys. Rev. B **97**, 125153 (2018).

[34] G. D. las Cuevas and T. S. Cubitt, Simple universal models capture all classical spin physics, Science **351**, 1180 (2016).

[35] K. Kim, S. Korenblit, R. Islam, E. E. Edwards, M.-S. Chang, C. Noh, H. Carmichael, G.-D. Lin, L.-M. Duan, C. C. J. Wang, J. K. Freericks, and C. Monroe, Quantum simulation of the transverse Ising model with trapped ions, New J. Phys. **13**, 105003 (2011).

[36] H. Bernien, S. Schwartz, A. Keesling, H. Levine, A. Omran, H. Pichler, S. Choi, A. S. Zibrov, M. Endres, M. Greiner, V. Vuletić, and M. D. Lukin, Probing many-body dynamics on a 51-atom quantum simulator, Nature (London) **551**, 579 (2017).

[37] M. R. Garey and D. S. Johnson, *Computers and Intractability: A Guide to the Theory of NP-Completeness* (Freeman, San Francisco, 1979), Vol. 174.

[38] F. Barahona, On the computational complexity of Ising spin glass models, J. Phys. A: Math. Gen. **15**, 3241 (1982).

[39] Y. Fu and P. W. Anderson, Application of statistical mechanics to NP-complete problems in combinatorial optimisation, J. Phys. A: Math. Gen. **19**, 1605 (1986).

[40] X. Qiu, P. Zoller, and X. Li, Programmable quantum annealing architectures with Ising quantum wires, PRX Quantum **1**, 020311 (2020).

[41] M. Kim, K. Kim, J. Hwang, E.-G. Moon, and J. Ahn, Rydberg quantum wires for maximum independent set problems, Nat. Phys. **18**, 755 (2022).

[42] M.-T. Nguyen, J.-G. Liu, J. Wurtz, M. D. Lukin, S.-T. Wang, and H. Pichler, Quantum optimization with arbitrary connectivity using Rydberg atom arrays, arXiv:2209.03965.

[43] A. Perdomo-Ortiz, S. E. Venegas-Andraca, and A. Aspuru-Guzik, A study of heuristic guesses for adiabatic quantum computation, Quantum Inf. Process. **10**, 33 (2011).

[44] N. Chancellor, Modernizing quantum annealing using local searches, New J. Phys. **19**, 023024 (2017).

[45] M. Ohkuwa, H. Nishimori, and D. A. Lidar, Reverse annealing for the fully connected p-spin model, Phys. Rev. A **98**, 022314 (2018).

[46] Y. Yamashiro, M. Ohkuwa, H. Nishimori, and D. A. Lidar, Dynamics of reverse annealing for the fully connected p-spin model, Phys. Rev. A **100**, 052321 (2019).

[47] J. Marshall, D. Venturelli, I. Hen, and E. G. Rieffel, Power of Pausing: Advancing Understanding of Thermalization in Experimental Quantum Annealers, Phys. Rev. Appl. **11**, 044083 (2019).

[48] P. T. Brown, D. Mitra, E. Guardado-Sanchez, R. Nourafkan, A. Reymbaut, C.-D. Hébert, S. Bergeron, A.-M. S. Tremblay, J. Kokalj, D. A. Huse, P. Schauß, and W. S. Bakr, Bad metallic transport in a cold atom Fermi-Hubbard system, Science **363**, 379 (2019).

[49] C. S. Chiu, G. Ji, A. Bohrdt, M. Xu, M. Knap, E. Demler, F. Grusdt, M. Greiner, and D. Greif, String patterns in the doped Hubbard model, Science **365**, 251 (2019).

[50] D. Greif, G. Jotzu, M. Messer, R. Desbuquois, and T. Esslinger, Formation and Dynamics of Antiferromagnetic Correlations in Tunable Optical Lattices, Phys. Rev. Lett. **115**, 260401 (2015).

[51] L. W. Cheuk, M. A. Nichols, K. R. Lawrence, M. Okan, H. Zhang, E. Khatami, N. Trivedi, T. Paiva, M. Rigol, and M. W. Zwierlein, Observation of spatial charge and spin correlations in the 2D Fermi-Hubbard model, Science **353**, 1260 (2016).

[52] J. H. Drewes, L. A. Miller, E. Cocchi, C. F. Chan, N. Wurz, M. Gall, D. Pertot, F. Brennecke, and M. Köhl, Antiferromagnetic Correlations in Two-Dimensional Fermionic Mott-Insulating and Metallic Phases, Phys. Rev. Lett. **118**, 170401 (2017).

[53] C. Hofrichter, L. Riegger, F. Scazza, M. Höfer, D. R. Fernandes, I. Bloch, and S. Fölling, Direct Probing of the Mott Crossover in the SU(n) Fermi-Hubbard Model, Phys. Rev. X **6**, 021030 (2016).

[54] M. Greiner, O. Mandel, T. Esslinger, T. W. Hänsch, and I. Bloch, Quantum phase transition from a superfluid to a Mott

insulator in a gas of ultracold atoms, Nature (London) **415**, 39 (2002).

[55] R. Landig, L. Hruby, N. Dogra, M. Landini, R. Mottl, T. Donner, and T. Esslinger, Quantum phases from competing short- and long-range interactions in an optical lattice, Nature (London) **532**, 476 (2016).

[56] N. Gemelke, X. Zhang, C.-L. Hung, and C. Chin, *In situ* observation of incompressible Mott-insulating domains in ultracold atomic gases, Nature (London) **460**, 995 (2009).

[57] F. Meinert, M. J. Mark, E. Kirilov, K. Lauber, P. Weinmann, M. Gröbner, A. J. Daley, and H.-C. Nägerl, Observation of many-body dynamics in long-range tunneling after a quantum quench, Science **344**, 1259 (2014).

[58] P. Jordan and E. Wigner, Über das Paulische äquivalenzverbot, Z. Phys. **47**, 631 (1928).

[59] I. Hen and F. M. Spedalieri, Quantum Annealing for Constrained Optimization, Phys. Rev. Appl. **5**, 034007 (2016).

[60] L. Hormozi, E. W. Brown, G. Carleo, and M. Troyer, Nonstoquastic Hamiltonians and quantum annealing of an Ising spin glass, Phys. Rev. B **95**, 184416 (2017).

[61] T. Albash, Role of nonstoquastic catalysts in quantum adiabatic optimization, Phys. Rev. A **99**, 042334 (2019).

[62] K. Takada, Y. Yamashiro, and H. Nishimori, Mean-field solution of the weak-strong cluster problem for quantum annealing with stoquastic and non-stoquastic catalysts, J. Phys. Soc. Jpn. **89**, 044001 (2020).

[63] E. Crosson, T. Albash, I. Hen, and A. P. Young, De-signing Hamiltonians for quantum adiabatic optimization, Quantum **4**, 334 (2020).

[64] K. Takada, S. Sota, S. Yunoki, B. Pokharel, H. Nishimori, and D. A. Lidar, Phase transitions in the frustrated Ising ladder with stoquastic and nonstoquastic catalysts, Phys. Rev. Res. **3**, 043013 (2021).

[65] D. A. Abanin, E. Altman, I. Bloch, and M. Serbyn, Colloquium: Many-body localization, thermalization, and entanglement, Rev. Mod. Phys. **91**, 021001 (2019).

[66] M. Lubasch, V. Murg, U. Schneider, J. I. Cirac, and M.-C. Bañuls, Adiabatic Preparation of a Heisenberg Antiferromagnet Using an Optical Superlattice, Phys. Rev. Lett. **107**, 165301 (2011).

[67] C. S. Chiu, G. Ji, A. Mazurenko, D. Greif, and M. Greiner, Quantum State Engineering of a Hubbard System with Ultracold Fermions, Phys. Rev. Lett. **120**, 243201 (2018).

[68] J. Lin, J. Nan, Y. Luo, X.-C. Yao, and X. Li, Quantum Adiabatic Doping with Incommensurate Optical Lattices, Phys. Rev. Lett. **123**, 233603 (2019).

[69] T. F. Rønnow, Z. Wang, J. Job, S. Boixo, S. V. Isakov, D. Wecker, J. M. Martinis, D. A. Lidar, and M. Troyer, Defining and detecting quantum speedup, Science **345**, 420 (2014).

[70] Q. Zhuang, Increase of degeneracy improves the performance of the quantum adiabatic algorithm, Phys. Rev. A **90**, 052317 (2014).

[71] S. Bravyi, D. P. Divincenzo, R. Oliveira, and B. M. Terhal, The complexity of stoquastic local Hamiltonian problems, Quantum Inf. Comput. **8**, 361 (2008).

[72] D. Guéry-Odelin, A. Ruschhaupt, A. Kiely, E. Torrontegui, S. Martínez-Garaot, and J. G. Muga, Shortcuts to adiabaticity: Concepts, methods, and applications, Rev. Mod. Phys. **91**, 045001 (2019).

[73] K. Takahashi, Shortcuts to adiabaticity for quantum annealing, Phys. Rev. A **95**, 012309 (2017).

[74] A. Hartmann and W. Lechner, Rapid counter-diabatic sweeps in lattice gauge adiabatic quantum computing, New J. Phys. **21**, 043025 (2019).

[75] G. Passarelli, V. Cataudella, R. Fazio, and P. Lucignano, Counterdiabatic driving in the quantum annealing of the p-spin model: A variational approach, Phys. Rev. Res. **2**, 013283 (2020).

[76] L. Prielinger, A. Hartmann, Y. Yamashiro, K. Nishimura, W. Lechner, and H. Nishimori, Two-parameter counter-diabatic driving in quantum annealing, Phys. Rev. Res. **3**, 013227 (2021).

[77] G. Passarelli, R. Fazio, and P. Lucignano, Optimal quantum annealing: A variational shortcut-to-adiabaticity approach, Phys. Rev. A **105**, 022618 (2022).

[78] T. Jörg, F. Krzakala, J. Kurchan, and A. C. Maggs, Simple Glass Models and Their Quantum Annealing, Phys. Rev. Lett. **101**, 147204 (2008).

[79] M. H. S. Amin and V. Choi, First-order quantum phase transition in adiabatic quantum computation, Phys. Rev. A **80**, 062326 (2009).

[80] T. Jörg, F. Krzakala, G. Semerjian, and F. Zamponi, First-Order Transitions and the Performance of Quantum Algorithms in Random Optimization Problems, Phys. Rev. Lett. **104**, 207206 (2010).

[81] E. Farhi, D. Gosset, I. Hen, A. W. Sandvik, P. Shor, A. P. Young, and F. Zamponi, Performance of the quantum adiabatic algorithm on random instances of two optimization problems on regular hypergraphs, Phys. Rev. A **86**, 052334 (2012).

[82] S.-J. Gu, Fidelity approach to quantum phase transitions, Int. J. Mod. Phys. B **24**, 4371 (2010).

[83] S. Knysh, Zero-temperature quantum annealing bottlenecks in the spin-glass phase, Nat. Commun. **7**, 12370 (2016).

[84] S. F. Edwards and P. W. Anderson, Theory of spin glasses, J. Phys. F **5**, 965 (1975).

[85] N. Linden, S. Popescu, A. J. Short, and A. Winter, Quantum mechanical evolution towards thermal equilibrium, Phys. Rev. E **79**, 061103 (2009).

[86] A. J. Short and T. C. Farrelly, Quantum equilibration in finite time, New J. Phys. **14**, 013063 (2012).

[87] E. Iyoda, H. Katsura, and T. Sagawa, Effective dimension, level statistics, and integrability of Sachdev-Ye-Kitaev-like models, Phys. Rev. D **98**, 086020 (2018).

[88] S. Iyer, V. Oganesyan, G. Refael, and D. A. Huse, Many-body localization in a quasiperiodic system, Phys. Rev. B **87**, 134202 (2013).

[89] X. Li, S. Ganeshan, J. H. Pixley, and S. Das Sarma, Many-Body Localization and Quantum Nonergodicity in a Model with a Single-Particle Mobility Edge, Phys. Rev. Lett. **115**, 186601 (2015).

[90] B. Altshuler, H. Krovi, and J. Roland, Anderson localization makes adiabatic quantum optimization fail, Proc. Natl. Acad. Sci. USA **107**, 12446 (2010).